# Spectral Analysis of Solar Radio Type III Bursts from 20 kHz to 410 MHz

K. Sasikumar Raja, Milan Maksimovic, Eduard P. Kontar, Xavier Bonnin, Philippe Zarka, Laurent Lamy, Hamish Reid, Nicole Vilmer, Alain Lecacheux, Vratislav Krupar, et al.

The Astrophysical Journal, 924:58 (9pp), 2022 January 10 https://doi.org/10.3847/1538-4357/ac34ed


# Spectral Analysis of Solar Radio Type III Bursts from 20 kHz to 410 MHz

K. Sasikumar Raja[1,2], Milan Maksimovic[1], Eduard P. Kontar[3], Xavier Bonnin[1], Philippe Zarka[1,4], Laurent Lamy[1,4,5], Hamish Reid[6], Nicole Vilmer[1,4], Alain Lecacheux[1], Vratislav Krupar[7,8], Baptiste Cecconi[1,4], Lahmiti Nora[1], and Laurent Denis[4]

[1] LESIA, Observatoire de Paris, Université PSL, Sorbonne Université, Université de Paris, CNRS, 92190 Meudon, France; sasikumar.raja@iiap.res.in, sasikumarraja@gmail.com
[2] Indian Institute of Astrophysics, II Block, Koramangala, Bangalore-560 034, India
[3] School of Physics and Astronomy, University of Glasgow, Glasgow G12 8QQ, UK
[4] Unité scientifique de Nançay, Observatoire de Paris, CNRS, PSL, Université d'Orléans/OSUC, Nançay, France
[5] Aix Marseille Univ, CNRS, CNES, LAM, Marseille, France
[6] Department of Space & Climate Physics, University College London, London, UK
[7] Goddard Planetary Heliophysics Institute, University of Maryland, Baltimore County, Baltimore, MD 21250, USA
[8] Heliophysics Science Division, NASA Goddard Space Flight Center, Greenbelt, MD 20771, USA
*Received 2021 June 6; revised 2021 October 8; accepted 2021 October 19; published 2022 January 12*

## Abstract

We present the statistical analysis of the spectral response of solar radio type III bursts over the wide frequency range between 20 kHz and 410 MHz. For this purpose, we have used observations that were carried out using both spaced-based (Wind/Waves) and ground-based (Nançay Decameter Array and Nançay Radioheliograph) facilities. In order to compare the flux densities observed by the different instruments, we have carefully calibrated the data and displayed them in solar flux units. The main result of our study is that type III bursts, in the metric to hectometric wavelength range, statistically exhibit a clear maximum of their median radio flux density around 2 MHz. Although this result was already reported by inspecting the spectral profiles of type III bursts in the frequency range 20 kHz–20 MHz, our study extends such analysis for the first time to metric radio frequencies (i.e., from 20 kHz to 410 MHz) and confirms the maximum spectral response around 2 MHz. In addition, using a simple empirical model we show that the median radio flux $S$ of the studied data set obeys the polynomial form $Y = 0.04X^3 - 1.63X^2 + 16.30X - 41.24$, with $X = \ln(F_{\rm MHz})$ and with $Y = \ln(S_{\rm SFU})$. Using the Sittler and Guhathakurtha model for coronal streamers, we have found that the maximum of radio power therefore falls in the range 4 to 10 $R_\odot$, depending on whether the type III emissions are assumed to be at the fundamental or the harmonic.

*Unified Astronomy Thesaurus concepts:* Solar corona (1483); Solar coronal radio emission (1993); Solar wind (1534)

## 1. Introduction

Solar type III radio bursts are produced by electron beams that are propagating along open magnetic field lines in the corona and interplanetary medium (IPM). Among the other radio bursts classified by Wild (1950, 1967), type IIIs are the most intense, fast drifting (0.1–0.5 $c$, where $c$ is the speed of light), and frequently observed bursts. It is widely accepted that type III bursts originate via a plasma emission mechanism (Ginzburg & Zhelezniakov 1958) in which the fast electrons form an unstable velocity distribution leading to a bump-on-tail instability (Bohm & Gross 1949) that excites Langmuir waves at the local plasma frequency ($f_p = 8.98 \times \sqrt{N_e}$, where $f_p$ is the plasma frequency in kHz and $N_e$ is the electron density in cm$^{-3}$). These Langmuir waves are then transformed into electromagnetic radiations by plasma emission mechanisms (Ginzburg & Zhelezniakov 1958). For instance, the coalescence of Langmuir waves and low-frequency ion–sound waves can produce radiation at the electron plasma frequency ($f_p$) called fundamental or F-emission, whereas the coalescence of two Langmuir waves can lead to radiation at the frequency $\approx 2f_p$ called harmonic or H-emission (Stewart 1974; Melrose 1987; Robinson et al. 1994; Thejappa & MacDowall 2018; Sasikumar Raja & Ramesh 2013; Mahender et al. 2020). As the electron density and therefore the plasma frequency decreases radially outward, type III bursts drift from high frequencies ($f_p \approx 1$ GHz) in the low corona down to the local plasma frequency of the observer, $f_p \approx 20$ kHz at 1 au. It has been known for a long time that type IIIs are extremely variable, both in radio flux density and in observing frequency range (Weber 1978; Dulk et al. 1984). A statistical study of type III bursts (Bonnin 2008b) observed by the Wind/Waves instrument (Bougeret et al. 1995) have also found a maximum response of type III bursts at around 1 MHz previously reported by Weber (1978). More recently, using the S/Waves instruments on board STEREO twin spacecraft (Bougeret et al. 2008; Kaiser et al. 2008), Krupar et al. (2014) have confirmed the statistical maximum of flux density around 1 MHz. In this article, we have studied the spectral response of the type III bursts over a much wider bandwidth (i.e., 20 kHz–410 MHz) and found that the maximum spectral response lies between 1 and 2 MHz. Furthermore, this study confirms that there are no other local maximum of the radio flux in the analyzed frequency bandwidth.

Several physical ingredients (e.g., electron density, electron beam speed, and beam density) and mechanisms determine the radio flux density of a type III burst and its variation with frequency. Variation of the flux density can be related to the

**Table 1**
Data Sets from Wind/Waves, Nancay Decameter Array, and Nancay Radioheliograph Used in the Study

| Data Set | Instrument | Observed Frequency | Observed Period | No. of Type III Bursts Observed |
|---|---|---|---|---|
| Data set I | Wind/Waves (RAD1 and RAD2) | 20 kHz–13.825 MHz | 1995–2009 | 1434 |
| Data set II | Wind/Waves (RAD1 and RAD2) and Nançay Decameter Array | 20 kHz–13.825 MHz & 10–80 MHz | 2013–2014 | 115 |
| Data set III | Nançay Radioheliograph | 150–450 MHz | 2002–2011 | 218 |

total energy and beam density of the interplanetary energetic flare electrons (Dulk et al. 1984). In addition, the local density fluctuations and/or turbulence can affect the energy of the beam and Langmuir waves (Nishikawa & Ryutov 1976; Muschietti et al. 1985).

In their study Krupar et al. (2014) have proposed a simple model in which the radio emission is at harmonic and saturated with a radio flux density proportional to the energy of Langmuir waves (Melrose 1980). If the latter is a simple function of the electron density and energy distribution, then the notable change of density gradient of the corona/solar wind in the 2 to 5 $R_\odot$ radial range (Sittler & Guhathakurta 1999) creates a maximum of the type III radio flux densities at around 1 MHz. However, the latter model does not fit the median flux density radial profile perfectly from Krupar et al. (2014).

In the present article, we have extended for the first time the studies by Bonnin (2008b), Lecacheux (2000), and Krupar et al. (2014) to metric–kilometric radio frequencies by combining the radio observations from space (Wind/Waves) with those from the ground-based Nançay Decameter Array (NDA; Boischot et al. 1980; Lecacheux 2000) and Nançay Radioheliograph (NRH; Kerdraon & Delouis 1997; Mercier et al. 2006) that are located at the Station de Radioastronomie de Nançay, France (latitude 47°23′ N; longitude 2°12′ E; altitude 150 m). By doing so, we extend the study of variation of the flux density with the frequency of type III bursts up to 410 MHz. Consequently, we provide new constraints on the physical mechanism that defines the radio flux density of type III bursts and its variation with frequency.

In Section 2 of this article, we describe the various radio instruments that are used for this study. Also, we focus on the techniques that are used for calibrating the observed voltage power spectral densities into radio density flux in physical units. In Section 3 the obtained results are presented along with the interpretations and discussions. Finally in Section 4, we provide a summary and conclusions.

## 2. Instruments, Observations, and Data Analysis

In this article, we have studied the spectral profiles of isolated type III bursts observed using different instruments briefly presented here. Based on the observing periods, locations and instruments, we have categorized them into three cases. The first one, henceforth data set I, contains type III bursts that are observed using the Waves instrument (Bougeret et al. 1995), on board the Wind spacecraft located at L1, irrespective of their longitudinal source location in the corona. This can even include type IIIs generated by electron beams originating on the opposite side of the Sun, as seen from L1. The second data set, henceforth data set II, contains type III bursts that are simultaneously observed by Wind/Waves at L1 and by the ground-based Nançay Decameter Array (Boischot et al. 1980). Finally, the third data set, henceforth data set III, contains imaging observations of type III bursts that are carried out using the NRH (Reid & Vilmer 2017). The details of the three data sets, including the frequency ranges of observations, are summarized in Table 1. Data set I consists of 1434 type III bursts that were observed during 1995–2009. Data set II consists of 115 type III bursts that were observed during 2013–2014. Data set III consists of 218 type III bursts observed during 2002–2011. In this case, Wind/Waves, NDA, and NRH are observing type III bursts that are generated on the visible side of the Sun with respect to the line-of-sight (LOS) direction.

In the following section, we briefly present the radio instruments used in this study, together with the irrespective calibration techniques.

### 2.1. Wind/Waves

The Wind/Waves experiment (Bougeret et al. 1995) has three electric dipole antennas; two of them are coplanar and orthogonal wire dipole antennas in the spin plane, whereas the other is a rigid spin-axis dipole. The longer dipole of Waves experiment ($E_x$) is of $2 \times 50$ m tip to tip and the other spin-plane dipole ($E_y$) length is $2 \times 7.5$ m tip to tip. The length of spin-axis dipole ($E_z$) is $2 \times 6$ m tip to tip. The Wind spacecraft spins at 20 turns per minute (i.e., 1 rotation in 3 s). Among others, the Waves experiment has two radio receiver bands, namely, radio receiver band–1 (RAD1) and radio receiver band–2 (RAD2).

RAD1 is designed to operate from 20 to 1040 kHz (sweeping a bandpass filter 3 kHz). RAD2 operates from 1.075 to 13.825 MHz (sweeping a bandpass filter of 20 kHz). Both RAD1 and Rad2 have 256 channels with a sensitivity of 7 nV $Hz^{-1/2}$. In this article, we use the observations carried out in S mode, i.e., one receiver is connected to $E_z$ and the other to the sum of $E_z$ and the shorter antenna ($E_y$) signals. The calibration technique we have used is described as follows.

The observed voltage power spectral density $P_{\rm obs}$ (in units of $V^2\,Hz^{-1}$) by the RAD1 and RAD2 receivers can be represented as

$$P_{\rm obs} = P_{\rm burst} + P_{\rm rec} + P_{\rm gal}, \quad (1)$$

where $P_{\rm burst}$ is the voltage power spectral density that corresponds to the radio emission from the Sun that we are interested in, $P_{\rm rec}$ is the receiver noise, and $P_{\rm gal}$ is the voltage power spectral density that corresponds to the galactic background. In order to measure $P_{\rm burst}$, we have to subtract both $P_{\rm rec}$ and $P_{\rm gal}$ from $P_{\rm obs}$. We know that the measurements of $P_{\rm rec}$ that were carried out from the ground were contaminated by electromagnetic interference in the laboratory. Therefore, before deployment of the antennas (i.e., from space after the launch), the receiver noise was measured and is subtracted from $P_{\rm obs}$ accordingly.

In order to have the true flux density of the galactic background ($S_{\rm gal}$ in $\rm W\,m^{-2}\,Hz^{-1}$), we used the galactic background model of Novaco & Brown (1978):

$$S_{\rm gal} = S_{g0} \times f_{\rm MHz}^{-0.76} e^{-\tau} \times \Omega, \quad (2)$$

where $S_{g0} = 1.38 \times 10^{-19}\,\rm W\ m^{-2}\ Hz^{-1}\ sr^{-1}$, $f_{\rm MHz}$ is the observed frequency in MHz, and $\Omega = 8\pi/3$ sr is the radio beam of the dipole in the short wavelength approximation.

We then calibrated the observed flux in $\rm V^2\,Hz^{-1}$ to $\rm W\,m^{-2}\,Hz^{-1}$ using the approach by Zarka et al. (2004) and Zaslavsky et al. (2011) and using the formula

$$S_{\rm wg} = (P_{\rm obs} - P_{\rm rec}) \times \frac{S_{\rm gal}}{P_{\rm gal}^{\rm obs}}, \quad (3)$$

where $S_{\rm wg}$ is the flux density in $\rm W\,m^{-2}\,Hz^{-1}$ with contribution from the galactic background included and $P_{\rm gal}^{\rm obs}$ is the observationally derived galactic background by inspecting large data set. After the calibration, we measured the flux density of the radio burst $S_{\rm burst}$ by subtracting $S_{\rm gal}$:

$$S_{\rm burst} = S_{\rm wg} - S_{\rm gal}. \quad (4)$$

### 2.2. Nançay Decameter Array

The NDA observes quasi-daily intense radio bursts from the solar corona over 10–80 MHz (Boischot et al. 1980; Lecacheux 2000; Lamy et al. 2017, 2021). It is a phased array consisting of 144 helical antennas (with a height of 9 m and diameter of 5 m) divided into two subarrays that are sensitive to left-handed (LCP) and right-handed circular polarization (RCP). Each subarray (with 72 antennas) is further divided into nine blocks with eight antennas in each group. The so-called Routine swept-frequency backend receiver used in this study has been continuously in operation since 1990. It records a full spectrum successively from each polarized subarray every 0.5 s, with 400 frequency channels (when covering 10–80 MHz, this yields a 175 kHz spectral step). It records alternative polarizations from one spectrum to the next. This study used Routine raw data expressed in dB of input voltage power spectral density in $\rm V^2\,Hz^{-1}$, sampled over 8 bits, and calibrated using the pipeline described below. NDA measurements include hourly calibration sequences, during which each block is unplugged from its eight-antenna set and connected to a noise diode of known flux instead. Such calibration sequences can be inverted to calibrate the raw data into absolute flux densities (De la Noë et al. 1979). Note that this method does not include the response of the antenna themselves but provides a fair first-order calibration (see Lecacheux 2000).

Each noise diode delivers $41.2 \pm 0.3\,dB_{\rm ENR}$, which, summed over the nine blocks of each subarray, yields a total flux of $50.75 \pm 0.9\,dB_{\rm ENR}$ (L. Denis 2019, personal communication). A calibration sequence decomposes into $4 \times 10$ s long intervals, during which the diode signal is sampled with a 0, 10, 20, and 30 dB attenuation. These calibration measurements can thus be inverted to derive the equivalent antenna temperature following the equation:

$$T_A \approx T_o \times 10^{dB_{\rm ENR}/10}\,\rm K, \quad (5)$$

where $T_o$ is the ambient temperature ($\approx$290 K). The antenna temperature can then be converted into flux density using

$$S = \frac{2k_B(T_A - T_{\rm sys})}{A_e}\ \ \rm W\,m^{-2}\,Hz^{-1}, \quad (6)$$

where, $k_B$ is the Boltzmann constant ($\simeq 1.38 \times 10^{-23}\,\rm JK^{-1}$), $A_e$ is the total effective area modeled by the NDA team, and $T_{sys}$ is the system temperature that we estimated for this study to be $\approx$17, $400 \pm 4000$ K. This calibration pipeline was applied separately for LCP and RCP data. The sum of LCP and RCP calibrated flux densities finally provides the total flux density (Stokes parameter I).

### 2.3. Nançay Radioheliograph

The NRH (Kerdraon & Delouis 1997; Mercier et al. 2006) is a two-dimensional imaging instrument that is capable of observing up to 10 frequencies in the range 150–450 MHz. The NRH is a T-shaped interferometer with 19 antennas in the east–west direction spread over 3200 m and 24 antennas in the north–south direction over 2440 m. After the year 2003, the number of antennas was increased to 48. In this work, we used the observations that are carried out at frequencies 164, 236, 327, and 410 MHz. At these frequencies, the flux density of type III bursts is calculated using routines that generate cleaned images of the burst.[9] The flux density is measured over a square window of size $440'' \times 440''$ around the location of maximum radio brightness and over an integration time of 10 s. It is worth mentioning that the radio galaxy Cygnus A (an intense radio source with known brightness) is used to calibrate the images. As Cygnus A is an extended source, an analytical model of the source is determined. Then the complex visibility function is derived with an accuracy of a few percent up to the highest spatial frequency of both arrays ($\approx 200\,\rm rad^{-1}$). The instrumental phase and gain fluctuations are about 5° and 5%, respectively.

## 3. Results and Discussions

### 3.1. Peak Spectral Response of Type III Bursts at 1.5 to 2 MHz

After calibrating all the events in data sets I, II, and III, they have been inspected to measure the maximum flux densities of the type III bursts for each observing frequency for each event. For instance, Figure 1 shows a typical calibrated dynamic spectrogram of a type III burst observed simultaneously by Wind/Waves (20 kHz–13.825 MHz) and NDA (10–80 MHz) on 2014 July 31. For this event, which belongs to data set II, we have determined the peak flux density of the type III burst for every single frequency channel that was recorded during the time interval 13:10–13:25 UT. Figure 2 shows the distribution of these maxima as a function of the observing frequency. The dotted vertical line indicates the frequency below which the signal corresponds to the electron quasi-thermal noise (QTN) detected by the antenna (Meyer-Vernet & Perche 1989). Considering frequencies above this dotted line, a global maximum flux density at $\approx$2 MHz can be seen.

Similarly, we have repeated this method and plotted the spectral response of the 1434 type III bursts of data set I in Figure 3. The yellow cross and magenta plus markers indicate the measurements derived using RAD1 and RAD2 receivers,

[9] http://bass2000.obspm.fr/soft_guide.php

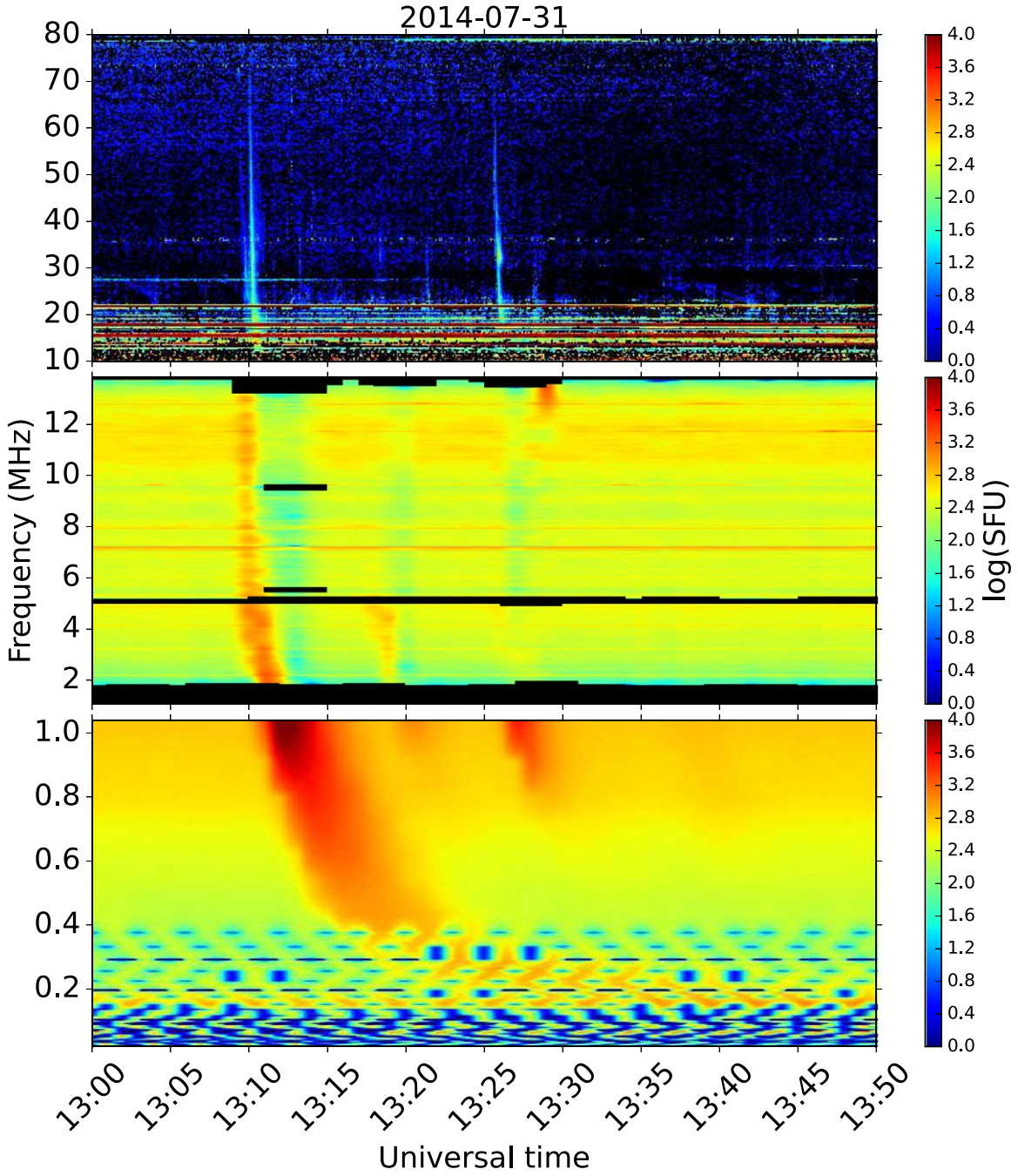


**Figure 1.** Calibrated dynamic spectrogram observed on 2014 July 31. The top panel shows the observation of type III bursts carried out using the Nançay Decameter Array in the frequency range 10–80 MHz. The middle and lower panels show observations carried out using the Wind/Waves instrument from space. The frequency range 20 kHz–1040 kHz (i.e., lower panel) is observed using RAD1 receiver, and the frequency range 1.075–13.825 MHz (i.e., middle panel) is carried out using RAD2 receiver. We note that a type III burst at 13:30 UT is not seen in RAD2 because of missing information.

respectively. The solid black curve represents, for each observing frequency, the median of the data points for all the events. The filled red region goes from first to third quartiles. As one can see, we confirm and refine the result already reported by Bonnin (2008b) and Krupar et al. (2014). When considering a large enough number of events, the typical type III radio emission exhibits a maximum at 1.5 to 2 MHz. In the studies by Bonnin (2008b) and Krupar et al. (2014) the maximum is close to 1 MHz, while in the present study, it is closer to 2 MHz. Furthermore, the flux at the spectral peak in Figure 3, which is $\approx 2 \times 10^4$ solar flux units (SFU; 1 SFU $= 10^{-22}$ W m$^{-2}$ Hz$^{-1}$), is almost the same as the maximum flux of $\approx 3 \times 10^4$ reported by Krupar et al. (2014) in their Figure 10.

Further, we have studied the peak flux densities of the 115 type III bursts of data set II. The outcome is displayed in Figure 4. The data points in yellow circles, magenta crosses, and blue pluses correspond the Wind/Waves/RAD1, Wind/Waves/RAD2, and the NDA, respectively. Again, the black solid curve represents the medians of the data points for all the events as a function of the frequency, and the filled red region indicates the first and third quartiles. Two remarks can be made on this figure. First, the spectral profile of the median type III

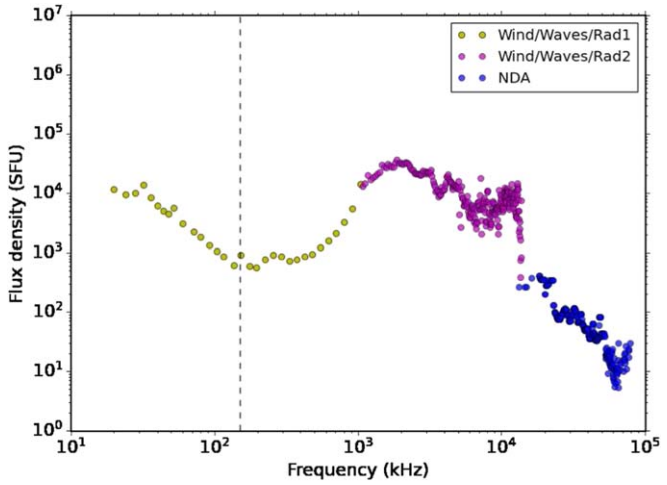


**Figure 2.** The maximum flux densities of type III bursts in different frequency channels that were observed simultaneously using Wind/Waves and NDA are shown for a typical event from data set II. The yellow, magenta, and blue markers indicate the measurements derived using Wind/Waves/RAD1, Wind/Waves/RAD2, and NDA instruments. The dotted vertical line delimits the range below ≈150 kHz where the signal is due to the plasma quasi-thermal noise detected by the antenna.

flux displayed in Figure 4 is globally continuous between Wind/Waves and the NDA, suggesting that our calibration techniques are reliable. Second, as for data set I, and despite fewer events, the median spectral profile of data set II also exhibits a maximum at about 1.5 MHz with a maximum flux of about $3 \times 10^4$ SFU. Even though it presents a more substantial variability as a function of frequency, the median spectral profile globally decreases from $3 \times 10^4$ SFU at 1.5 MHz to about $5 \times 10^2$ SFU at 80 MHz.

The more significant fluctuations in the 5–80 MHz frequency range can be attributed to (i) the resonance frequency of the half-wave dipole Wind/Waves antenna, (ii) radio frequency interference (RFI) from the spacecraft, (iii) the strong terrestrial RFI, and (iv) the ionospheric absorption. Indeed, a relative decrease in the flux density is seen from 10 to 40 MHz in Figure 4.

In addition to the Wind/Waves and the NDA data, we have overplotted in Figure 4 the peak flux densities of type III bursts measured using imaging observations of the NRH, i.e., data set III. These data are displayed by orange asterisk markers. As before, the black solid curve in the 150–450 MHz range represents the medians of the NRH data points for all the events, and the filled reddish region indicates the first and third quartiles. As for the NRH frequency range, the median type III radio flux decreases as a frequency function in the NRH range. As data sets II and III do not correspond to the same statistical samples of solar type III radio bursts, we can consider that these two samples are representative of the mean evolution of radio power of type III bursts with the frequency. Therefore, we show, for the first time, that the typical type III radio flux decreases continuously from $3 \times 10^4$ SFU at 1.5 MHz to about 5 SFU at 400 MHz.

### 3.2. Summary of Our Statistical Analysis

Before presenting the summary of our analysis and displaying the profiles of the medians of the peak fluxes, we have to remove the QTN contribution at low frequencies and discuss the uncertainties of our measurements. Above the plasma frequency and for an antenna of length much longer than the local Debye length, which is the case for the Wind spacecraft, the QTN varies as $f^{-3}$ for $f \gg f_p$ (Meyer-Vernet & Perche 1989; Meyer-Vernet et al. 2000). For frequencies $f \gtrsim f_p$ the variation is less steep and is roughly $f^{-0.5}$ in the case of Wind. At 1 au, the plasma frequency typically varies between 10 and 40 kHz. Therefore, it is reasonable to assume that for the 20 to 150 kHz range (where we see the QTN in our data; see Figures 3 and 4), QTN varies as a power law with a spectral index between the two cases mentioned above. Therefore, instead of removing the QTN from each single spectrum, we have subtracted by fitting the median data curves below 150 kHz with the following empirical power-law model:

$$S_{\rm SFU} = S_0 \times (f/f_0)^{\alpha}\ , \tag{7}$$

where $S_{\rm SFU}$ is the flux density in SFU, $S_0$ is the flux density corresponding to the starting frequency of observations (i.e., $f_0 = 20$ kHz), $f$ is the frequency of observations below 150 kHz, and $\alpha$ is the power-law index. The power-law index we obtain for both data sets is $\alpha \approx -1.3$, which is well in the expected range $[-3, -0.5]$. Figure 6 shows the spectral response of the type III bursts after QTN is removed.

Concerning the uncertainties of our measurements, we have made the following assumption. For an observable $x$ that is normally distributed, the uncertainty on the mean value $\langle x \rangle$ of a sample of $N$ measurements of $x_i$ is $\sigma_x/\sqrt{N}$, where $\sigma_x$ is the standard deviation of all the $x_i$. However, our radio fluxes $S_i$ are represented by log-normal distributions and not by normal ones. The distributions of $\log(S_i)$ are close to normal as shown in the panels (a)–(d) of Figure 5. The panels show the RAD1 (708.0 kHz), RAD2 (1625 kHz), NDA (71 MHz), and NRH (410 MHz) observations. Also, this can be seen in Figures 3 and 4 where the filled red regions indicate the first and third quartiles are symmetric with respect to the median values. Furthermore, the medians and means of the distribution of $\log(S_i)$ are similar, which is not the case of the medians and means of $S_i$. Thus, the error bars must be computed over $\log(S_i)$ distributions.

Figure 6 presents, therefore, the summary of our statistical analysis. It displays the median radio fluxes profiles of both data set I (Figure 3) in red and data sets II and III (Figure 4) in blue. For these profiles, we have removed the QTN at low frequencies and added the error bars in log scale, defined as $\sigma_{\log(S)}/\sqrt{N}$, where $\sigma_{\log(S)}$ are the standard deviations of $\log(S_i)$ for all frequencies. For the Wind/Waves frequency range, as the standard deviations are similar for data sets I and II, the error bars are smaller for data set I because of the larger number of samples (1434 instead of 115).

As indicated in Table 1, the three data sets do not correspond to the same period of the solar cycle. Data set I covers observations from 1995 to 2009, which correspond to the full solar cycle 23, while data set II covers a period of solar cycle 24 restricted to only the maximum of this cycle, which occurred in mid-2014. As far as data set III is concerned, it covers a period spanning from the declining phase of solar cycle 23 up to the maximum of solar cycle 24. These different solar cycle coverages suggest that, whatever the observation period, as long as the number of type III considered is large enough, we observe the same behavior of the maximum of the radio flux as a function of the frequency. Namely, the maximum of radio emission at about 2 MHz is an intrinsic property of the type III generation at decametric to kilometric

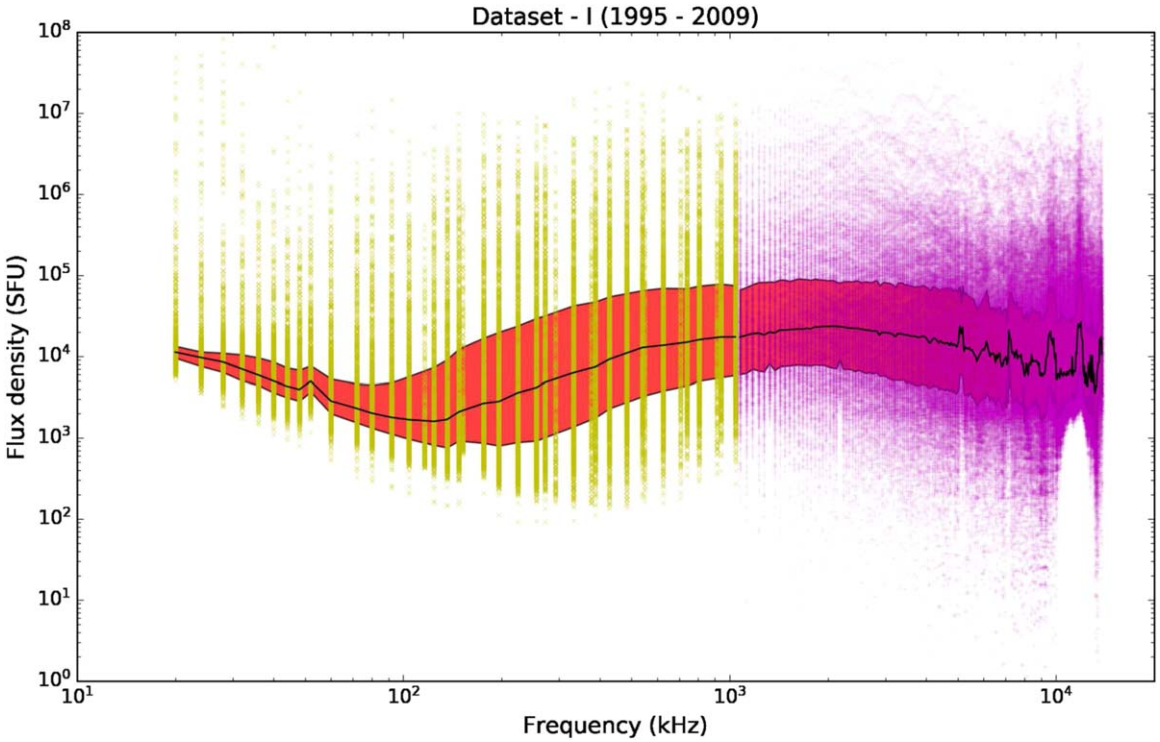


**Figure 3.** Maximum flux density of type III bursts that were observed during 1995–2009 is shown. The yellow cross and magenta plus markers indicate the observations of RAD1 and RAD2 receivers, respectively. The black solid curve represents the median (i.e., 50th percentile) of the peak flux densities of the data shown in every frequency channel. Red filled region shows the first and third quartiles of the data shown. Note that the galactic contribution is subtracted as described in Section 2.

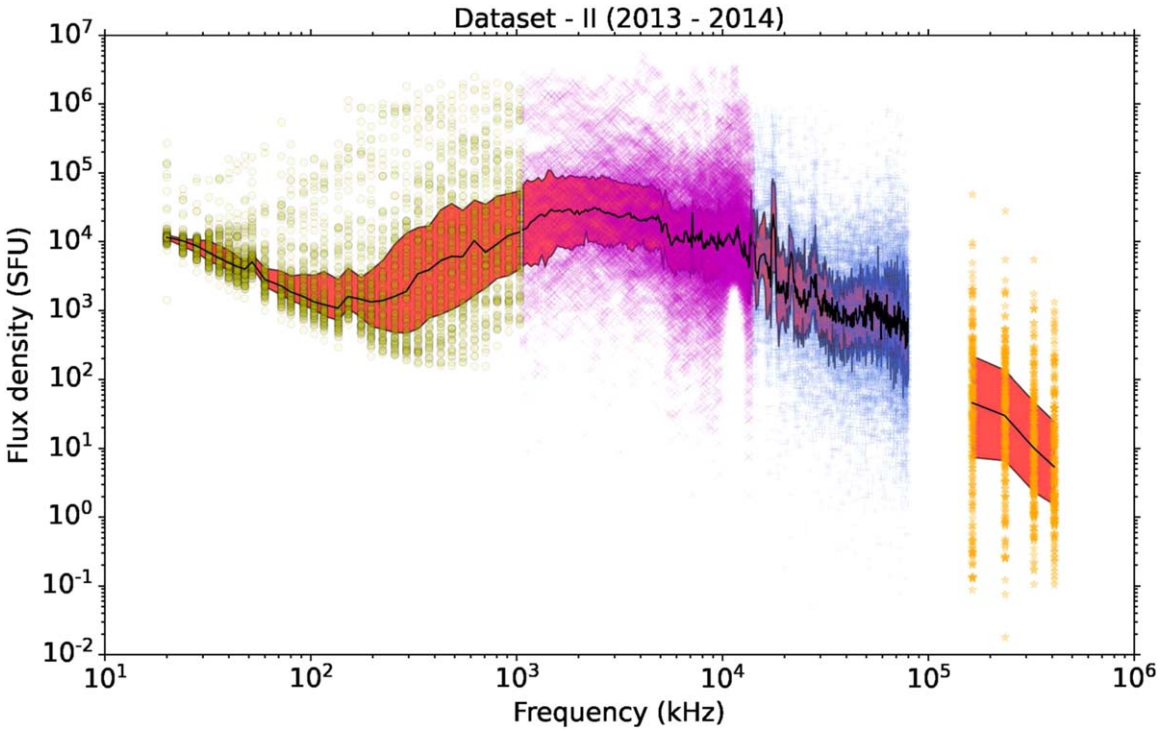


**Figure 4.** Spectral response of type III bursts observed from 20 kHz to 410 MHz is shown. The yellow circle, magenta cross, and blue plus markers indicate the maximum flux density (in SFU) of the 115 type III bursts observed using RAD1 and RAD2 receivers of the Wind/Waves instrument and Nançay Decameter Array, respectively. The orange asterisk markers indicate the observations of Nançay Radioheliograph at selected frequencies (i.e., 164, 236, 327, and 410 MHz). The black solid curve represents the median (i.e., 50th percentile) of the flux densities of the data shown in every frequency channel. The red filled region shows the first and third quartiles of the data shown. Note that the galactic contribution is subtracted as described in Section 2.

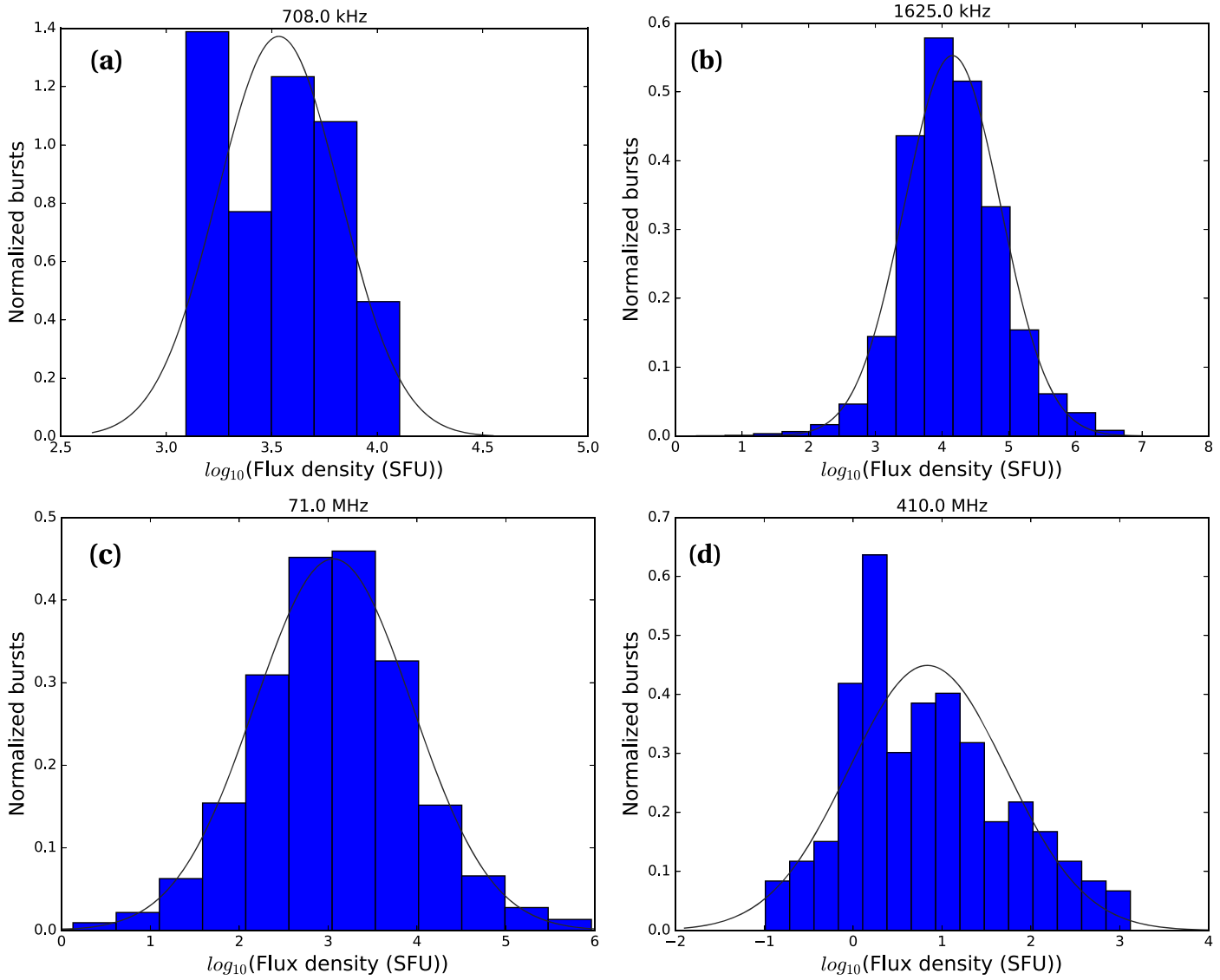


**Figure 5.** Panels (a), (b), (c), and (d) show the log-normal distribution of flux density of type III bursts observed by RAD1, RAD2, NDA, and NRH, respectively. A black curve indicates the normal distribution of the logarithm of flux densities.

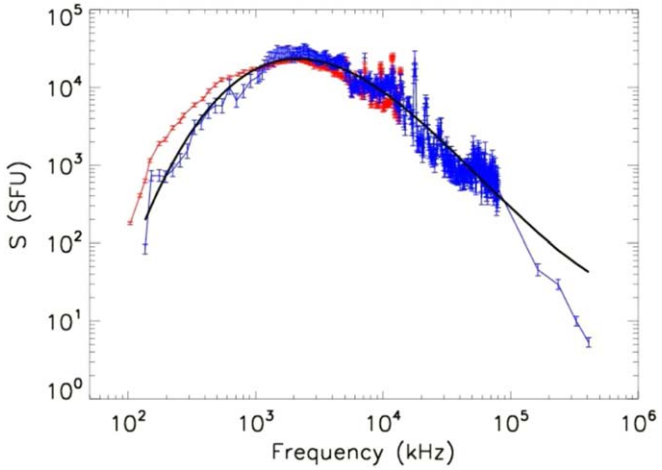


**Figure 6.** Median curves from Figures 3 (derived using data set I in red) and 4 (derived using data sets II and III in blue) after removing the quasi-thermal noise detected by the antennas below 150 kHz and computing the error bars. The black solid line represents the empirical polynomial model of $Y = \ln(S_{\rm SFU})$ as a function of $X = \ln(F_{\rm MHz})$ (see the text for more details).

wavelengths. This property seems to be confirmed even in the metric range since the radio fluxes of data set III are also decreasing as a function of the frequency and are well below the fluxes observed by the NDA in the decametric range. We have therefore confirmed and fine-tuned the initial observations by Weber (1978), Bonnin (2008b), and Krupar et al. (2014), by extending them for the first time up to the metric frequency range. In order to quantify this main result and make it usable for future theoretical studies, we have fitted the data from the data sets II and III with a three-order polynomial model and obtained that the empirical model that best represents the observations is

$$Y = 0.04X^3 - 1.63X^2 + 16.30X - 41.24 \quad (8)$$

with $X = \ln(F_{\rm MHz})$ and $Y = \ln(S_{\rm SFU})$. This model is represented in Figure 6 by the black solid line.

A final remark concerning Figure 6 is that the blue and red curves overlap, within the error bars, at all frequencies above 1 MHz. Below 1 MHz, the radio fluxes are slightly lower for data set II than for data set I, even though the global evolution is the same, namely, a decrease of the flux as a function of the

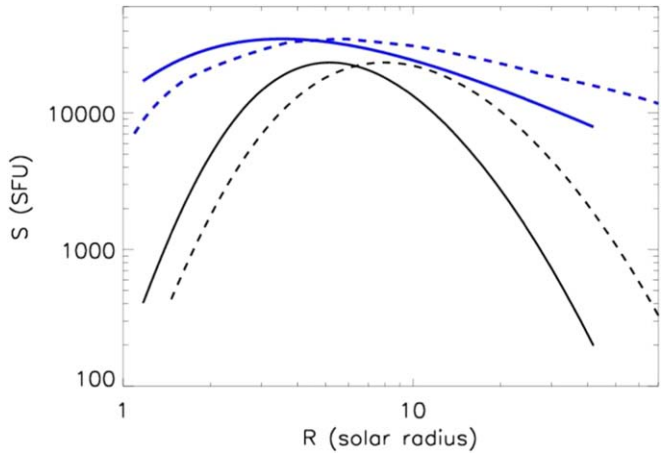


**Figure 7.** The same median fluxes as those shown in Figure 6 are displayed as a function of the distance from the Sun. Here we use the Sittler and Guhathakurta model for coronal streamers (Sittler & Guhathakurta 1999) and assume a fundamental emission for type III bursts (black solid line) or the harmonic (black dashed line). The solid and dashed lines represent tentative explanations of the median radio flux (see the text for more details).

decreasing frequency in this range. This behavior is a bit puzzling and is under investigation.

### *3.3. Possible Explanations for the Maximum of the Radio Flux Density of Type III Bursts*

Assuming a density model for the corona and solar wind, it is possible to locate the maximum of the radio flux density of type III bursts. Using the Sittler and Guhathakurta model for coronal streamers (Sittler & Guhathakurta 1999) and assuming a fundamental emission for type III bursts, the black solid line in Figure 7 displays the previously found empirical model of the radio radio flux as function of the distance from the Sun and given by Equation (8).

Note, however, that there is a possibility that the maximum of type III emissions we observe is a combination of both fundamental and harmonic emissions Krupar et al. (2014). The black dashed line in Figure 7 represents the same empirical model for the radio flux, assuming an emission at the harmonic of the plasma frequency for the type IIIs. The maximum of radio power falls therefore in the range 4 to 10 $R_\odot$ (from the center of the Sun) depending whether the emission is assumed to be at the fundamental or the harmonic. This radial range is crucial for the solar wind since this is where it becomes both supersonic, after the Parker sonic point, and super-Alfvénic.

Krupar et al. (2014) have proposed a simple model in which the radio emission is at harmonic and saturated with a radio flux density proportional to the energy of Langmuir waves (Melrose 1980). Assuming a fast relaxation of the energetic electron beam as in Kontar (2001), Krupar et al. (2014) obtain that the radio flux is simply proportional to $1/(r^2 f_p)$ (see their Equation (12)). Figure 7 shows the Krupar et al. (2014) model by a blue solid line. As can be seen, the maximum of the radio flux for this model is somewhat below the maximum of the observed radio fluxes.

Given that the density fluctuations could affect the growth of Langmuir waves, the type III radio generation will be influenced by the density fluctuations in the corona and solar wind. This, in turn, could affect the location of the maximum of the observed radio fluxes. Specifically, the generation of Langmuir waves could be suppressed by a higher level of density fluctuations, so the maximum is shifted with respect to the simplified model by Krupar et al. (2014). There are no in situ observations of the density fluctuations in the outer corona. The only current possibility is to model and/or simulate the evolution of the plasma turbulence in this region and to assume that the density fluctuations have a suitable trend. An additional complication connected with density turbulence is the scattering of radio waves between the source and observer. The scattering broadens the burst time profile and hence can reduce the peak flux detected at 1 au.

Nevertheless, a full comprehensive model that could explain in detail why there is a maximum of the type III radio power around 5–6 $R_\odot$ is still to be found.

## 4. Summary and Conclusions

In this article, we have performed the first ever statistical analysis of the spectral response of solar type III bursts over the wide frequency range between 20 kHz and 410 MHz. For this purpose, we have used the observations that were carried out using both spaced-based (Wind/Waves) and ground-based (Nançay Decameter Array and Nançay Radioheliograph) facilities. In order to compare the flux densities observed by the different instruments, we have carefully calibrated the data and displayed them in solar flux units. We have studied 1434 type III bursts that were observed by Wind/Waves solely (see 3) and 115 type III bursts that were observed simultaneously by both Wind/Waves and NDA (see Figure 4). Note that in the latter case, both instruments observed type III bursts that were roughly in the same line of sight. In addition, we have included the data derived using calibrated observations of the NRH at some specific frequencies.

The main results of our study is that type III bursts in the metric to hectometric wavelengths range statistically exhibit a maximum of their radio power at around 1 to 2 MHz. Using the Sittler and Guhathakurtha model for coronal streamers (Sittler & Guhathakurta 1999), we have found that this frequency range corresponds to the heliocentric distance range ≈3–8 $R_\odot$ if one assume a radio emission at the fundamental plasma frequency. On the other hand if the type III bursts are a combination of both fundamental and harmonic emissions, the maximum of the radio flux would originate in the heliocentric distance range of ≈1 to 20 $R_\odot$. This radial range is crucial for the solar wind since this is where it becomes both supersonic, after the Parker sonic point, and super-Alfvénic.

Finally, there is no doubt that our findings will soon be compared to in situ observations. Indeed the Parker Solar Probe (Fox et al. 2016) is expected to reach 10 $R_\odot$ in 2024. The in situ measurements of the various plasma parameters including density fluctuations, Langmuir waves, and energetic electrons should provide crucial information for fully explaining the maximum radio flux of solar type III bursts.

K.S.R. acknowledges the financial support from the Centre National d'études Spatiales (CNES), France. V.K. acknowledges the support by NASA under grants 18-2HSWO218_2-0010 and 19-HSR-19Z_2-0143. The authors acknowledge the Nançay Radio Observatory/Unité Scientifique de Nançay of the Observatoire de Paris (USR 704-CNRS, supported by Université d'Orléans, OSUC, and Région Centre in France) for providing access to NDA observations accessible online at http://www.obs-nancay.fr (see Lamy et al. 2021). The NRH is funded by the French Ministry of Education and the Région

Centre. French coauthors were supported by the CNRS/INSU PNST program. We thank the referee for providing useful suggestions that helped in improving the manuscript.

## ORCID iDs

Milan Maksimovic https://orcid.org/0000-0001-6172-5062
Eduard P. Kontar https://orcid.org/0000-0002-8078-0902
Xavier Bonnin https://orcid.org/0000-0003-4217-7333
Philippe Zarka https://orcid.org/0000-0003-1672-9878
Laurent Lamy https://orcid.org/0000-0002-8428-1369
Hamish Reid https://orcid.org/0000-0002-6287-3494
Nicole Vilmer https://orcid.org/0000-0002-6872-3630
Vratislav Krupar https://orcid.org/0000-0001-6185-3945
Baptiste Cecconi https://orcid.org/0000-0001-7915-5571

## References

Bohm, D., & Gross, E. P. 1949, PhRv, 75, 1864
Boischot, A., Rosolen, C., Aubier, M. G., et al. 1980, Icar, 43, 399
Bonnin, X. 2008b, PhD thesis, Université Paris-Diderot—Paris VII, https://hal.archives-ouvertes.fr/tel-00461521
Bougeret, J. L., Goetz, K., Kaiser, M. L., et al. 2008, SSRv, 136, 487
Bougeret, J. L., Kaiser, M. L., Kellogg, P. J., et al. 1995, SSRv, 71, 231
De la Noë, J., Rosolen, C., & Couteret, J. 1979, Calibration of the Decametric Network II: Electronic Systems (Paris: Paris Observatory)
Dulk, G. A., Steinberg, J. L., & Hoang, S. 1984, A&A, 141, 30
Fox, N. J., Velli, M. C., Bale, S. D., et al. 2016, SSRv, 204, 7
Ginzburg, V. L., & Zhelezniakov, V. V. 1958, SvA, 2, 653
Kaiser, M. L., Kucera, T. A., Davila, J. M., et al. 2008, SSRv, 136, 5
Kerdraon, A., & Delouis, J.-M. 1997, The Nançay Radioheliograph, Vol. 483 (Berlin: Springer), 192
Kontar, E. P. 2001, A&A, 375, 629
Krupar, V., Maksimovic, M., Santolik, O., et al. 2014, SoPh, 289, 3121
Lamy, L., Le Gall, A., Cecconi, B., et al. 2021, Nançay Decameter Array (NDA) Solar Routine observation data collection v1.7, PADC/CDN, doi:10.25935/ZZV2-PE64
Lamy, L., Zarka, P., Cecconi, B., et al. 2017, in Proc. of the 8th Int. Workshop, Planetary Radio Emissions VIII, ed. G. Fischer et al. (Vienna: Austrian Academy of Sciences Press), 455
Lecacheux, A. 2000, GMS, 119, 321
Mahender, A., Sasikumar Raja, K., Ramesh, R., et al. 2020, SoPh, 295, 153
Melrose, D. B. 1980, SSRv, 26, 3
Melrose, D. B. 1987, SoPh, 111, 89
Mercier, C., Subramanian, P., Kerdraon, A., et al. 2006, A&A, 447, 1189
Meyer-Vernet, N., Hoang, S., Issautier, K., Moncuquet, M., & Marcos, G. 2000, GMS, 119, 67
Meyer-Vernet, N., & Perche, C. 1989, JGR, 94, 2405
Muschietti, L., Goldman, M. V., & Newman, D. 1985, SoPh, 96, 181
Nishikawa, K., & Ryutov, D. D. 1976, JPSJ, 41, 1757
Novaco, J. C., & Brown, L. W. 1978, ApJ, 221, 114
Reid, H. A. S., & Vilmer, N. 2017, A&A, 597, A77
Robinson, P. A., Cairns, I. H., & Willes, A. J. 1994, ApJ, 422, 870
Sasikumar Raja, K., & Ramesh, R. 2013, ApJ, 775, 38
Sittler, E. C. J., & Guhathakurta, M. 1999, ApJ, 523, 812
Stewart, R. T. 1974, SoPh, 39, 451
Thejappa, G., & MacDowall, R. J. 2018, JPhCS, 1100, 012026
Weber, R. R. 1978, SoPh, 59, 377
Wild, J. P. 1950, AuSRA, 3, 541
Wild, J. P. 1967, PASAu, 1, 38
Zarka, P., Cecconi, B., & Kurth, W. S. 2004, JGRA, 109, A09S15
Zaslavsky, A., Meyer-Vernet, N., Hoang, S., Maksimovic, M., & Bale, S. D. 2011, RaSc, 46, RS2008